

A Novel Low-Cost Channel Sounder for Double-Directionally Resolved Measurements in the MmWave band

Hussein Hammoud¹, Yuning Zhang¹, Zihang Cheng¹, Seun Sangodoyin²,
Hofer Markus³, Faruk Pasic⁴, Thomas M. Pohl⁴, Radek Závorka⁵, Ales Prokes⁵,
Thomas Zemen³, *Senior Member, IEEE*, Christoph Mecklenbräuer⁴, *Senior Member, IEEE*,
Andreas F. Molisch¹, *Fellow, IEEE*

¹ University of Southern California, Los Angeles, CA, USA,

² Georgia Institute of Technology, Atlanta, GA, USA,

³ AIT Austrian Institute of Technology, Austria,

⁴ Technische Universität Wien, Vienna, Austria,

⁵ Brno University of Technology, Czech Republic

Abstract—With the move towards 6G and associated technology deployment in higher frequency bands, measurements of directionally-resolved channels and sounders capable of performing such measurements are a necessity. In this paper, we present a new concept of channel sounding based on a *Redirecting Rotating Mirror Arrangement* (ReRoMA), capable of performing double-directional channel measurements at millimeter wave frequencies by mechanical beam steering orders of magnitude faster than existing rotating-horn arrangements. We present this new concept, describe a prototype operating at 60 GHz, and use it to perform, as proof-of-principle, a dynamic cart-to-cart channel measurements at a T-intersection scenario. We show that this sounding principle works and allows the directional evaluation of the channel. We visualize the different resolvable propagation paths in terms of dynamic angular and delay power spectrum, and relate them to the environmental geometry.

Index Terms—channel measurements, double-directional, channel modelling, mmWave, dynamic channels, V2V, 6G

I. INTRODUCTION

Since 2010, the wireless communication industry has seen a massive move to higher frequency bands. This is motivated by the large available bandwidth in those bands, and is reflected both in the use of mmWave bands for 5G deployment and the anticipated use of (sub)THz bands in 6G. With any such move comes the prerequisite of understanding the wireless propagation channel in these new frequency bands. Measuring parameters such as path loss, shadowing, delay dispersion and angular spreads is essential for any reasonable system development and testing.

A well-known fact however is that with the move towards higher frequency bands, communication suffers from increased propagation losses, and beamforming becomes a necessity to compensate for it [1, Chapter 4, 16]. Hence directionally resolved channel measurements and models are required. The process of exciting the channel of interest with a known signal into different directions and estimating, for each such

transmit direction, the channel impulse responses arriving from different directions at the receiver, is what we refer to as double-directional channel sounding.

For the determination of directional information, channel sounders require the use of antenna arrays. While real, switched, or switched-beam arrays allow very fast measurements [1, Chapter 9], often the cost, calibration, and availability of components are prohibitive. For this reason, virtual arrays, in particular mechanical rotation of horn antennas by stepper motors, are popular especially at high frequencies [2], [3]. However, they are slow because of the required mechanical movement, usually with a stepper motor, between the different antenna positions. Additionally, high-frequency hardware is sensitive to mechanical influences on the cabling, e.g., the twisting of cables as the horn rotates. Rotary joints offer a solution for this problem, however come at high cost especially above 40 GHz, and furthermore, they are fault-prone for long continuous operation [4]. While mounting the whole sounder on a rotating platform solves the cabling problem, it only achieves relatively slow rotation speeds (max 300 RPM) and has only been implemented for narrowband sounding [5], [6] at 28 and 60 GHz respectively.

To overcome these challenges, the current paper presents a novel channel sounder whose key idea is the separation of the electronic signal generation/transmission part, which remains static, and a beamsteering part that is rotating. Specifically, the beamsteering is realized by a fast-spinning *Redirecting Rotating Mirror Arrangement* (ReRoMA) [7], see Sec. II-A for a detailed description of the setup. The concept is implemented on both link ends in a carefully coordinated way, allowing fast double-directional channel measurements. Specifically, a full MIMO snapshot can be measured within 1 s, which is orders of magnitude faster than traditional rotating-horn setups, and allows to measure a dynamic channel within its stationarity

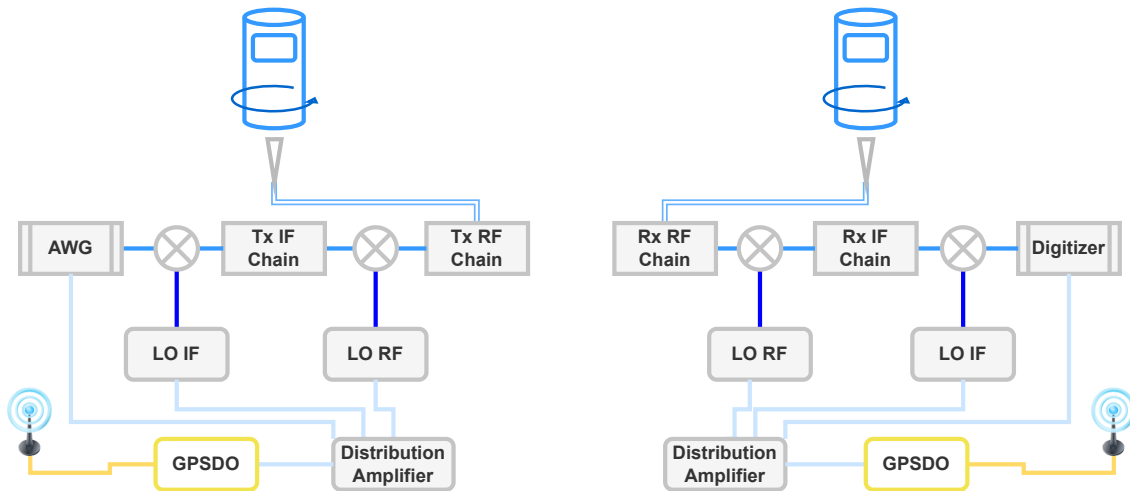


Fig. 1. High-level schematic ReRoMa channel sounder diagram

time, and do that with a low cost and calibration complexity.¹

Thus, the main contributions of this paper are:

- We introduce a new concept for channel sounding based on ReRoMA that provides a new tradeoff between measurement speed, cost/complexity, and need for specialized components, and in particular allows to retain the simplicity of rotating-horn sounders while increasing the measurement speed by orders of magnitude.
- We elucidate the components that make ReRoMA work and introduce a working prototype.
- We use this ReRoMA-based prototype sounder to perform a double-directional measurements at 60 GHz in a dynamic T-intersection scenario.

II. SOUNDER SETUP

A. ReRoMa

The mechanical structure of our system is based on two main components: a fixed object (FO) and a moving/rotating object (MO). The FO at the Tx includes all the electronics for the generation of the sounding signal at the desired frequency, which is ultimately transmitted from a horn antenna upwards (see Fig. 1). The task of the MO is to allow our sounder to automatically scan the full 360-degree azimuth plane, in a short period of time, and without any needed human intervention/adjustment. The system we have chosen for this task is a cylindrical tube that is rotated by a belt drive by a direct current (DC) motor see Fig. 2.

The cylindrical tube has a mirror angled at 45 degrees, reflecting the incident beam illuminated from the antenna sitting at the bottom of the tube, from a vertical incidence

¹The authors used a rotating device previously in [8]. However, that paper differs in both method and capability from the current approach. In [8], the excitation is by an omnidirectional antenna, and the beam is formed by a designed aperture in a hollow metallic half-sphere, while the current approach re-directs an already-existing beam. This beamforming half-sphere is rotatable which allows mechanical beam steering. That device was only designed for beamforming at one link end, and rotation is slow (full rotation on *one* link end took several seconds).

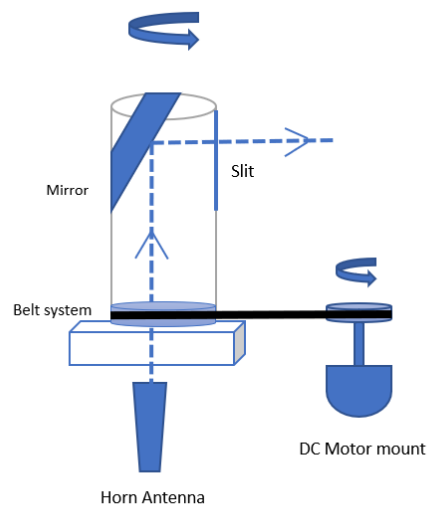


Fig. 2. ReRoMA sample configuration diagram

to a horizontal beam reflection, that goes through an open slit on the side of the tube.

Remark 1: In principle, the angle of the mirror can be arbitrary and could be changed depending on the scenario one is trying to measure. For example, a downward-reflection of the antenna beam could mimic a scenario where one of the ends is a base station (BS), typically with downward-tilt at an elevated height, communicating with ground-height devices.

Remark 2: The alignment of the horn antenna with respect to the rotating tube is essential, as one would want the antenna beam to illuminate the center of the reflecting mirror to allow a focused beam to be reflected out of the tube slit, without significant reflections and “waveguiding” happening inside the tube. For that to be achieved, a metallic mount was built that fixes the antenna element below the bottom of the rotating tube to allow fine alignment-adjustment for the antenna, based on

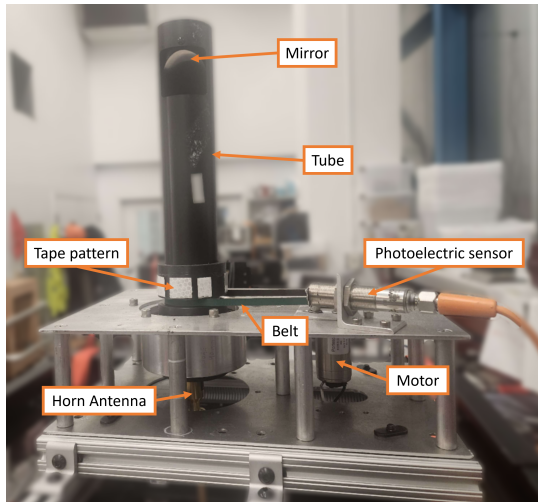


Fig. 3. ReRoMA implementation in hardware

a calibration measurement performed with a laser pointer.

The choice of rotation speeds between the Tx and Rx depends on a variety of factors such as the antennas' beamwidths, the desired multiple-input multiple-output (MIMO) snapshot time, and the number of virtual-array positions at both the Tx and the Rx. Starting from the Rx side, and based on a safety assessment of our proof-of-concept structure, we are able to safely and stably rotate the Rx at ~ 2080 rotations-per-minute (RPM), or equivalently 28 ms for a full Rx rotation. Using this rotation speed and performing a capture of the received sounding signal every $400 \mu\text{s}$, we sample the channel every 0.55 beamwidth (the 3 dB beamwidth of the Rx horn is 9°). This provides a total of 72 Rx positions (1 position every 5°) during one rotation. On the Rx side, we rotate more slowly, so that the Tx rotates 10° during one full rotation of the Rx. Thus, the number of "effective" distinct Tx positions are 36. Consequently, to preserve the rule of more than 1 capture per 3 dB beamwidth, we have used a different horn antenna on the Tx, with 3 dB beamwidth being 25° . With all of these parameters, we are able to capture a full single-input multiple-output (SIMO) snapshot every 28 ms and a full MIMO snapshot every 1 s, which implies that the Tx performs a full rotation about once per second, more precisely rotation is with 57 RPM. *Remark 3:* Note that though 1 s is less than typical stationarity times of channels (i.e., the time during which the channel statistics stay unchanged), it is larger than the coherence time (roughly equal to the inverse Doppler spread) of typical channels. This implies that the sounder cannot measure the Doppler spectrum.

To be able to construct a double-directional impulse response, we need to precisely match each captured received sounding signal) with the directions in which the Tx and Rx tubes are pointing at the time of capture. In our implementation, we have designed and built an optical photoelectric sensor system, with a polarized reflecting tape attached to the MO, and the sensor mounted on top of the FO. The use of the polarized tape was necessary to allow outdoor

measurements during day-time, due to their much higher resilience to ambient daylight. Note that we are only aiming to measure the orientation with this system, not to control it.

Although one piece of polarized tape on the rotating tube could be enough to get an estimate the orientation direction under the assumption of a uniform rotation speed, we further enhance the accuracy by cutting the polarized tape into a very specific coded pattern (coded based on the lengths of dark non-reflective vs. light reflective areas) on both the Tx and the Rx, that can be directly recognized in the captured sensor data, allowing a more accurate mapping between the sensor data and the actual physical orientation.

The sensor data are captured using National Instruments (NI) DAQ boards with different sampling rates at Tx and Rx, due to their different rotation speed. The sample rate of the Tx is 120 kS/s (kilo samples per second) and the rate for the Rx is 2.5 MS/s (Mega samples per second). This high sampling rate allows to capture the sensor reflections with time resolution of $8.3 \mu\text{s}$ and $0.4 \mu\text{s}$, which is more than enough to accurately represent the captured data from the reflective tapes on both sides. With every capture of the data, corresponding to 50 kS, we save a GPS-based timestamp to be used in post-processing to match the sensor data with the captured measurement data.

The polarization of the feeding horn is in principle arbitrary. However, it is advantageous to use circular polarization for the excitation, since for the case of linear polarization from the horn, the polarization vector of the redirected wave changes its orientation angle as a function of the mirror orientation.

In the case of using a circular polarization (as we are in our system), it is important to keep in mind that circular polarization flips handedness upon reflection, thus, in order to get a full representation of the channel, it is necessary to switch across the two directions of circular polarization - left handed circular polarization (LHCP) and right-handed circular polarization (RHCP) - on at least one of the two ends of our sounder (Tx or Rx). We choose to switch polarization on the Rx side (which leads to less demanding power handling capabilities) by a polarization switch; in our prototype this was the Mi-wave Series 145 polarization switch [9]).

B. Electronic components

We now turn to the generation and reception of the sounding signal. We note that the principle of our ReRoMA channel sounder is not tied to the specifics of these aspects, but rather the following description serves to understand the performance prototype and the measurement results achieved with it. A high-level schematic for our sounder can be seen in Fig. 1. As sounding signal, we employ a custom-designed orthogonal frequency division multiplexing (OFDM)-like multi-tone sequence, similar to the Zadoff-Chu sequences used in LTE, but with modifications that reduce the peak-to-average power ratio (PAPR) of filtered and oversampled signals. The bandwidth of the sounding signal is 200 MHz, constituted from 400 subcarriers, leading to 500 kHz subcarrier spacing, corresponding to maximum 600 m propagation distance that can be unambiguously determined; this is anticipated to be

more than enough for all the measured scenarios. Distance resolution, corresponding to the 200 MHz bandwidth, is 1.5 m. This sounding waveform is shifted digitally to passband; in other words, we consider a digital implementation that covers the frequency range from 200 – 400 MHz. This waveform is loaded onto an arbitrary waveform generator (AWG) prior to measurements, and is triggered once by the 1 PPS signal generated from a GPS-disciplined clock, then keeps on repeating indefinitely. A single repetition of this waveform lasts 2 μ s.

The AWG output is fed into a first mixer, upconverting the signal to a center frequency of 3.7 GHz, with the lower sideband occupying the 3.3 – 3.5 GHz range, and the upper sideband occupying the 3.9 – 4.1 GHz range, where the latter is suppressed by a filter. The lower sideband is fed into the second mixing stage, upconverting it to the designated RF band. Such a dual-stage heterodyne reduces the requirements on the Q-factor of the used filters [1, Chapter 17]. At the output of the second mixing stage, we use a band-pass filter to limit the transmitted frequencies to the 59 – 61 GHz band. At passband, we first feed the signal into a power amplifier, increasing the power to 22 dBm. At the output of the power amplifier, we install a polarizer that fixes the transmitted-signal polarization to LHCP. The output from the polarizer is then transmitted by a conical horn antenna, with a beamwidth of 25°.

On the Rx side, the signal is captured using a conical horn antenna with 9° beamwidth. The signal goes then into a polarization-switch/polarizer that can switch between LHCP and RHCP, followed by a bandpass filter and a low-noise amplifier (LNA), boosting the power by \sim 40 dB. The signal is then fed into a RF mixing stage, bringing it down to around 3.7 GHz intermediate frequency (IF). Another filtering stage is done at IF, before mixing it down to 300 MHz, amplifying it again using another LNA (to match the voltage swing of the digitizer), before it is finally captured and stored by a NI PXIe-5162 digitizer, for later processing. For more details about the RF chains and the used components refer to [10].

III. EVALUATIONS PROCEDURE

In line with the preceding sections, the objective of this study is to assess and characterize the double-directional channel between the Tx and Rx. The dynamic, complex double-directional channel transfer function can be expressed as the aggregate of contributions stemming from N multipath components (MPCs) [11]:

$$\begin{aligned} H(f, \varphi_{R,q}, \varphi_{T,p}) = & \sum_{l=1}^N \alpha_l b_T(\phi_{T,l} - \varphi_{T,p}, f) \\ & b_R(\phi_{R,l} - \varphi_{R,q}, f) e^{-j2\pi f \tau_l} \end{aligned} \quad (1)$$

where α_l , τ_l , $\phi_{T,l}$ and $\phi_{R,l}$ are the complex amplitude, propagation delay, direction-of-departure (DoD) and direction-of-arrival (DoA) of the l^{th} path, respectively, and $b_T(\varphi_{T,p}, f)$ and $b_R(\varphi_{R,q}, f)$ denote the complex antenna gain patterns of the transmitter and receiver, respectively, centered at the p^{th} and q^{th} orientations. In this context, the horn is oriented towards

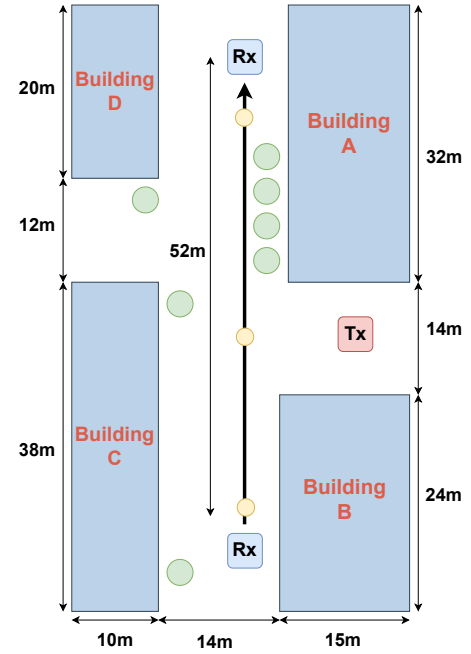


Fig. 4. Measurement environment

$\varphi_{T,p}$ and $\varphi_{R,q}$ for the transmitter and receiver, respectively. It is important to note that this model exclusively considers wave propagation in the horizontal plane, with no elevation consideration.

At time t , the received signal results from the convolution of the sounding sequence with both the channel impulse response and the system's (back-to-back) impulse response. This relationship can also be expressed as follows:

$$\begin{aligned} r_{\text{meas}}(t, \varphi_{R,q}, \varphi_{T,p}) &= \mathcal{F}_f^{-1} \{ R_{\text{meas}}(f, \varphi_{R,q}, \varphi_{T,p}) \} \\ &= \mathcal{F}_f^{-1} \{ H(f, \varphi_{R,q}, \varphi_{T,p}) H_{\text{B2B}}(f) X_{\text{wav}}(f) \} \end{aligned} \quad (2)$$

where \mathcal{F}_f^{-1} is the inverse fast Fourier transform (IFFT) with respect to f , $H_{\text{B2B}}(f)$ is the back-to-back transfer function of the system and $X_{\text{wav}}(f)$ is the sounding waveform.

In our measurement process, incorporating all the aforementioned considerations and leveraging the datasets obtained during the measurement campaign (comprising timestamped ADC captures and timestamped transmitter and receiver sensor data), we approximate the received signal \hat{r}_{meas} on a rectangular grid based on the measured sample values r_{meas} as follows:

$$\begin{aligned} \hat{r}_{\text{meas}}(nT_s, \hat{\varphi}_{R,q}, \hat{\varphi}_{T,p}) &= \mathcal{F}_f^{-1} \{ \hat{R}_{\text{meas}}(f, \hat{\varphi}_{R,q}, \hat{\varphi}_{T,p}) \} \\ &\approx r_{\text{meas}}[nT_s, \varphi_{R,q}, \varphi_{T,p}] \end{aligned} \quad (3)$$

where T_s is the ADC trigger period set at 200 μ s, and $(\hat{\varphi}_{R,q}, \hat{\varphi}_{T,p})$ are computed by projecting the measured angular orientations $(\omega_R(nT_s), \omega_T(nT_s))$ of the receiver and transmitter onto the nearest rectangular grid point $(\hat{\varphi}_{R,q}, \hat{\varphi}_{T,p})$. The spacing of the points in this rectangular grid equals the spacing of the adjacent horn orientations at transmitter and receiver, respectively, i.e., 10° for the transmitter and 5° for the receiver.

The measurement data for the two polarization directions can be organized into three-dimensional matrices, denoted as $\hat{\mathbf{R}}_{\text{meas|co}}(f_k, \hat{\varphi}_{R,q}, \hat{\varphi}_{T,p})$ and $\hat{\mathbf{R}}_{\text{meas|cross}}(f_k, \hat{\varphi}_{R,q}, \hat{\varphi}_{T,p})$. These matrices have dimensions $N_f \times N_{R_x} \times N_{T_x}$, where f_k represents the frequency index, and $\hat{\varphi}_{R,q}$, $\hat{\varphi}_{T,p}$ denote the rectangular-grid antenna positions obtained by projecting angular data. N_f denotes the number of frequency points, while N_{R_x} and N_{T_x} represent the total number of directions on the receiver and transmitter sides, respectively. Subsequently, we mitigate the effects of the system transfer function (the transfer function of our sounder) and the antenna patterns for both the transmitter and the receiver to derive the calibrated directional channel transfer function \mathbf{H} , given by:

$$\mathbf{H}(f_k, \hat{\varphi}_{R,q}, \hat{\varphi}_{T,p}) = \frac{\hat{\mathbf{R}}_{\text{meas|co}}(f_k, \hat{\varphi}_{R,q}, \hat{\varphi}_{T,p})}{\mathbf{H}_{\text{B2B|co}}(f_k) b_{\text{T}}(0, f_k) b_{\text{R}}(0, f_k)} + \frac{\hat{\mathbf{R}}_{\text{meas|cross}}(f_k, \hat{\varphi}_{R,q}, \hat{\varphi}_{T,p})}{\mathbf{H}_{\text{B2B|cross}}(f_k) b_{\text{T}}(0, f_k) b_{\text{R}}(0, f_k)}. \quad (4)$$

From this, the directional power delay profile (PDP) is computed as

$$P_{\text{direc}}(\tau, \hat{\varphi}_{R,q}, \hat{\varphi}_{T,p}) = |\mathcal{F}_{f_k}^{-1}\{\mathbf{H}(f_k, \hat{\varphi}_{R,q}, \hat{\varphi}_{T,p}) \cdot \mathbf{W}_{\text{hann}}(f_k)\}|^2 \quad (5)$$

where $\mathcal{F}_{f_k}^{-1}$ is the inverse fast Fourier transform (IFFT) with respect to f_k , and \mathbf{W}_{hann} is a Hann window applied in the frequency domain, which suppresses sidelobes in the delay domain at the expense of slightly broadening the main lobe of the impulse response. Finally, we apply noise thresholding and delay gating, similar to [12]:

$$P(\tau, \hat{\varphi}_{R,q}, \hat{\varphi}_{T,p}) = \begin{cases} P_{\text{direc}} & \text{if } (\tau \leq \tau_{\text{gate}}) \wedge (P_{\text{direc}} \geq P_{\lambda}) \\ 0 & \text{otherwise} \end{cases} \quad (6)$$

where τ_{gate} is the delay gating value selected to avoid using long delay points and points with “wrap-around” effect of the IFFT, and P_{λ} is the noise threshold. The thresholding eliminates noise-only delay bins, whose contributions would distort estimation of delay- and angular-dispersion parameters. For our current measurements, τ_{gate} is set to 250 m excess runlength, while P_{λ} is selected to be 6 dB above the average noise level of the PDP.

For analyzing the channel behavior from an “omni-directional” perspective, we synthesize the omni-PDPs by an approach similar to [13], i.e. by reconstructing the omni-directional pattern from the full double-directional capture by selecting the maximum power component (the direction of the highest contribution) per delay bin

$$P_{\text{omni}}(\tau) = \max_{\hat{\varphi}_{R,q}, \hat{\varphi}_{T,p}} P(\tau, \hat{\varphi}_{R,q}, \hat{\varphi}_{T,p}) \quad (7)$$

In addition, to analyze the channel behavior from an angular perspective, we generate the angular and delay power spectrum (ADPS) at both the Tx and the Rx as

$$\text{ADPS}_{\text{Tx}}(\tau, \hat{\varphi}_{T,p}) = \sum_{\hat{\varphi}_{R,q}} P(\tau, \hat{\varphi}_{R,q}, \hat{\varphi}_{T,p}) \quad (8)$$

$$\text{ADPS}_{\text{Rx}}(\tau, \hat{\varphi}_{R,q}) = \sum_{\hat{\varphi}_{T,p}} P(\tau, \hat{\varphi}_{R,q}, \hat{\varphi}_{T,p}) \quad (9)$$

IV. EXAMPLE MEASUREMENT

To verify the performance of our new sounding technique based on ReRoMA, we have measured a dynamic scenario where the Tx and Rx were mounted on carts (about 1.5 m above ground), and performed a measurement that mimics a car-to-car T-intersection environment. The measurement was performed on the campus of the University of Southern California (USC) in downtown Los Angeles, CA, USA; a map of the environment are shown in Fig. 4. The Tx stays stationary throughout the measurement, while the Rx starts from a non-line-of-sight (NLOS) position with respect to the Tx, and progresses along a linear track where it gets into a line-of-sight (LOS) scenario for a short period of time before going into NLOS again.

The first 8 seconds of this measurement scenario had the Rx stationary (for calibration purposes), after-which the Rx movement speed was fixed at 1 m/s. The total measurement time is 60 seconds.

Following the process of Sec. III, we evaluate the omni-PDP, where all delays are multiplied by speed of light, so that they correspond to distances. Sample results for 3 measurement positions indicated with yellow circles on Fig. 4 are shown in Fig. 5 where the main MPCs, their strengths and their corresponding delays are indicated. We move from a NLOS scenario in Fig. 5(a) (position 1) to a LOS scenario Fig. 5(b) (position 30) to again a NLOS scenario Fig. 5(c) (position 55), which is consistent with the fact that the first-arriving MPC is the strongest in Fig. 5(b) but not Figs. 5(a), (c). We also note that the delays seen in the PDPs accurately correspond to the delays expected from the environment. More specifically, for position 1, we observe a weak component coming at delay 25.5 m, which corresponds to the diffraction along the edge of building B. A much stronger component arrives at delay = 39 m, which corresponds to the component emitted from the Tx, reflected on building C before reaching the Rx. For position 30, we observe the LOS peak coming at delay = 12 m, as well as several MPCs caused by reflections of building C or reflections caused by the metallic lamp-posts signified by the green circles in Fig. 4. We go again into the NLOS scenario with position 55, where we see the weak diffraction around the edge of building A, in addition to the strong reflection caused by building D. We also show the dynamic PDP evolution vs. time in Fig. 6 where we can clearly see the position for which we have moved from NLOS into LOS and then back to NLOS again. Additionally, while we are under LOS conditions, we can observe the temporal side-lobes (stemming from the inverse Fourier transform of

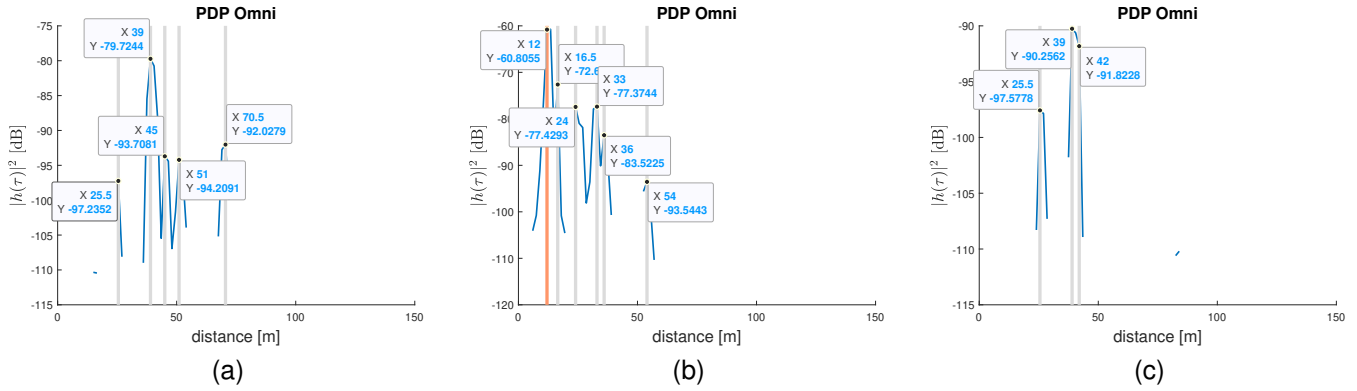


Fig. 5. Omni-PDP for the T intersection scenario at time (a) $t=0$ s (NLOS), (b) $t=30$ s (LOS), (c) $t=55$ s (NLOS)

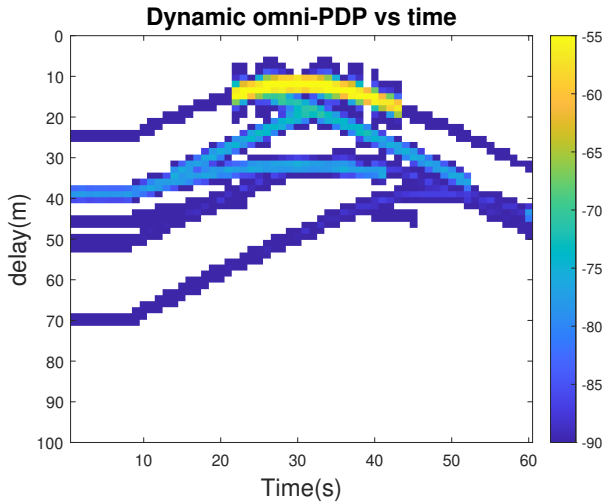


Fig. 6. Dynamic PDP evolution vs time

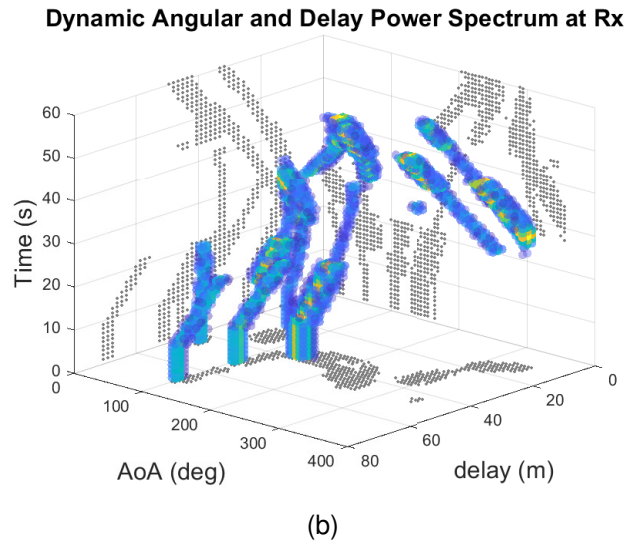
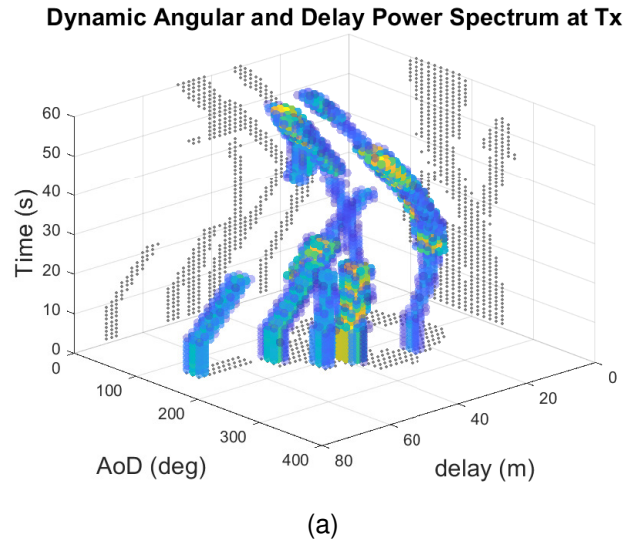


Fig. 7. Dynamic evaluation of the ADPS at (a) Tx, (b) Rx

the finite-support spectrum) seen before the delay of the LOS that are visible because of the LOS path being strong, and are therefore absent (eliminated by the thresholding) in the case where the quasi-LOS component is weak. Moreover, we are able to track the reflections off of the buildings, most notably buildings C and D.

We also show in Fig. 7 the dynamic evolution of the ADPS for both the Tx and the Rx. First of all, we clearly notice how each of the MPCs clusters can be dynamically tracked properly in angle and in delay without ambiguity. We also show in grey the projections of the ADPS on each of the planes, to allow for easier distinction of the tracks followed by each of the MPCs. The main contributing MPCs are the LOS path, the MPC reflected against building C, and the MPC reflected against building D. We can clearly see the birth and death for all of these clusters thus verifying the directional capabilities of our sounder.

V. CONCLUSION

In this paper, we have introduced a new concept for channel sounding based on our ReRoMA. Our prototype enables

scanning of full 360° range in azimuth at both the transmitter and the receiver, allowing the capture of a full MIMO 36×72

snapshot within the stationarity time of a dynamic channel. We have done a proof-of-concept measurement of a dynamic T-intersection scenario at 60 GHz and shown that we can directionally resolve the different propagation paths in angle and delay. This concept can also be easily extended to other frequency ranges; faster-evolving channels could be measured by adjusting the rotation and capture speeds.

Acknowledgement: Part of this work was supported by the California Transportation Authority under the METRANS program, and by the National Science Foundation.

REFERENCES

- [1] A. F. Molisch, *Wireless Communications: From Fundamentals to Beyond 5G*, 3rd ed. IEEE Press - Wiley, 2023.
- [2] T. S. Rappaport *et al.*, "Millimeter wave mobile communications for 5G cellular: It will work!" *IEEE Access*, vol. 1, pp. 335–349, 2013.
- [3] C. Han *et al.*, "Terahertz wireless channels: A holistic survey on measurement, modeling, and analysis," *IEEE Communications Surveys & Tutorials*, vol. 24, no. 3, pp. 1670–1707, 2022.
- [4] C. A. Fernandes *et al.*, "Review of 20 years of research on microwave and millimeter-wave lenses at" instituto de telecomunicaçoes," *IEEE Antennas and Propagation Magazine*, vol. 57, no. 1, pp. 249–268, 2015.
- [5] J. Du *et al.*, "Directional measurements in urban street canyons from macro rooftop sites at 28 GHz for 90% outdoor coverage," *IEEE Transactions on Antennas and Propagation*, vol. 69, no. 6, pp. 3459–3469, 2021.
- [6] N. Ntetsikas *et al.*, "60 GHz Outdoor to Indoor (O2I) propagation measurements in a university campus," in *2022 IEEE 23rd International Workshop on Signal Processing Advances in Wireless Communication (SPAWC)*. IEEE, 2022, pp. 1–5.
- [7] A. F. Molisch *et al.*, "Spinning directional antenna in centimeter and millimeter wave bands," Patent WO 2022155493 A1, sep 2022, available at: <https://patents.google.com/patent/WO2022155493A1/en>.
- [8] H. Groll *et al.*, "Scanning aperture antennas with spherical shells," in *2019 International Conference on Electromagnetics in Advanced Applications (ICEAA)*. IEEE, 2019, pp. 1220–1223.
- [9] Millimeter Wave Products Inc., "Waveguide polarization switch: Frequency 50 GHz - 75 GHz, cross polarization -20 db, 90 degrees or rh/lh polarization, 30 ma," Millimeter Wave Products Inc., 2023, accessed: 2023-11-08. [Online]. Available: <https://www.miww.com/waveguide-polarization-switch-frequency-50-ghz-75-ghz/>
- [10] H. Hammoud *et al.*, "A novel low-cost channel sounder for double-directionally resolved measurements in the mmwave band," *IEEE T. Wireless Comm.*, p. under review, 2024.
- [11] A. F. Molisch *et al.*, "Measurement of the capacity of mimo systems in frequency-selective channels," in *IEEE VTS 53rd Vehicular Technology Conference, Spring 2001. Proceedings (Cat. No. 01CH37202)*, vol. 1. IEEE, 2001, pp. 1–6.
- [12] N. A. Abbasi *et al.*, "THz band channel measurements and statistical modeling for urban d2d environments," *IEEE T. Wireless Comm.*, pp. 1466–1479, 2022.
- [13] S. Hur *et al.*, "Synchronous channel sounder using horn antenna and indoor measurements on 28 GHz," in *2014 IEEE International Black Sea Conference on Communications and Networking (BlackSeaCom)*. IEEE, 2014, pp. 83–87.